

## ATMOSPHERIC CIRCULATION AND CLOUD EVOLUTION ON THE HIGHLY ECCENTRIC EXTRASOLAR PLANET HD 80606B

NIKOLE K. LEWIS<sup>1,2</sup>, VIVIEN PARMENTIER<sup>3,8</sup>, TIFFANY KATARIA<sup>4</sup>, JULIEN DE WIT<sup>5</sup>, ADAM P. SHOWMAN<sup>3</sup>, JONATHAN J. FORTNEY<sup>6</sup>, MARK S. MARLEY<sup>7</sup>*Draft version May 8, 2018*

## ABSTRACT

Observations of the highly-eccentric ( $e \sim 0.9$ ) hot-Jupiter HD 80606b with *Spitzer* have provided some of the best probes of the physics at work in exoplanet atmospheres. By observing HD 80606b during its periapse passage, atmospheric radiative, advective, and chemical timescales can be directly measured and used to constrain fundamental planetary properties such as rotation period, tidal dissipation rate, and atmospheric composition (including aerosols). Here we present three-dimensional general circulation models for HD 80606b that aim to further explore the atmospheric physics shaping HD 80606b's observed *Spitzer* phase curves. We find that our models that assume a planetary rotation period twice that of the pseudo-synchronous rotation period best reproduce the phase variations observed for HD 80606b near periapse passage with *Spitzer*. Additionally, we find that the rapid formation/dissipation and vertical transport of clouds in HD 80606b's atmosphere near periapse passage likely shapes its observed phase variations. We predict that observations near periapse passage at visible wavelengths could constrain the composition and formation/advection timescales of the dominant cloud species in HD 80606b's atmosphere. The time-variable forcing experienced by exoplanets on eccentric orbits provides a unique and important window on radiative, dynamical, and chemical processes in planetary atmospheres and an important link between exoplanet observations and theory.

*Keywords:* atmospheric effects - methods: numerical - planets and satellites: general - planets and satellites: individual (HD 80606b)

## 1. INTRODUCTION

HD 80606b is a ‘hot Jupiter’ ( $M_p = 3.94 M_J$ ,  $R_p = 0.98 R_J$ ) on an extremely eccentric orbit ( $e = 0.9332$ ) (Pont et al. 2009). First discovered by Naef et al. (2001) using radial velocity observations, HD 80606b was later determined to be eclipsed by (Laughlin et al. 2009) and transit (Moutou et al. 2009) its host star. The extreme eccentricity of the orbit of HD 80606b is the result of ‘Kozai Migration’ in the presence of a binary star system (Wu & Murray 2003). During its  $\sim 111$  day orbit, HD 80606b experiences extreme ( $\sim 800\times$ ) shifts in the amount of incident flux it receives from its host star from apoapse to the periapse of its orbit. These variations in stellar insolation are likely to cause not only dramatic changes in the thermochemical structure of the planet, but also in global scale wind and cloud patterns.

Observations with the *Spitzer Space Telescope* (Werner et al. 2004) presented in de Wit et al. (2016) and Laughlin et al. (2009) have shown that HD 80606b exhibits large variations in its flux as a function of orbital phase near periapse passage. Such flux variations were predicted by atmospheric models for exoplanets on eccentric orbits, which exhibit significant variations in atmospheric temperature and wind speeds that directly inform atmospheric radiative and dynamical timescales (Langton & Laughlin 2008; Lewis et al. 2010; Cowan & Agol 2011; Kataria et al. 2013; Lewis et al. 2014). Laughlin et al. (2009) were the first to directly measure the atmospheric radiative timescale for an exoplanet with their *Spitzer* 8  $\mu\text{m}$  observations of HD 80606b. Through their 30 hour observation of HD 80606b near secondary eclipse, when the planet passes behind its host star, and periapse passage, Laughlin et al. (2009) estimated a radiative timescale of 4.5 hours near the 8  $\mu\text{m}$  photosphere of the planet.

Building on the original analysis of HD 80606b presented in Laughlin et al. (2009), de Wit et al. (2016) revisited the 8  $\mu\text{m}$  *Spitzer* observations given the recent evolution in data reduction techniques (e.g. Lewis et al. 2013) and performed a combined analysis with HD 80606b observations taken in the 4.5  $\mu\text{m}$  channel of *Spitzer* in 2009. The HD 80606b observations taken at 4.5  $\mu\text{m}$  provided a significantly longer temporal baseline around the periapse of HD 80606b's orbit, with 80 hours worth of data in total. This increased baseline allowed de Wit et al. (2016) to not only estimate the radiative timescales in HD 80606b's atmosphere near its 4.5 and 8  $\mu\text{m}$  photospheres ( $\sim 4$  hours), but also the atmospheric absorptivity at the pressures probed and the bulk rotation rate of the planet. de Wit et al. (2016) estimate the bulk rotation period of HD 80606b to be 93 hours, significantly longer than the predicted ‘pseudo-synchronous’ rotation period (Hut 1981) of  $\sim 40$  hours.

The interpretation of the HD 80606b phase variations observed by *Spitzer* presented in Laughlin et al. (2009) and de Wit et al. (2016) relied on semi-analytic (e.g. Cowan & Agol 2011; de Wit et al. 2016) and two-dimensional

<sup>2</sup> Department of Earth and Planetary Sciences, Johns Hopkins University, Baltimore, MD 21218, USA<sup>3</sup> Department of Planetary Sciences and Lunar and Planetary Laboratory, The University of Arizona, Tucson, AZ 85721, USA<sup>4</sup> Jet Propulsion Laboratory, California Institute of Technology, 4800 Oak Grove Drive, Pasadena, CA 91109, USA<sup>5</sup> Department of Earth, Atmospheric and Planetary Sciences, Massachusetts Institute of Technology, Cambridge, MA 02139, USA<sup>6</sup> Department of Astronomy & Astrophysics, University of California, Santa Cruz, CA 95064, USA<sup>7</sup> NASA Ames Research Center 245-3, Moffett Field, CA 94035, USA<sup>8</sup> Sagan Postdoctoral Fellow

hydrodynamical models (Langton & Laughlin 2008). Such models allow for rapid exploration of how specific changes in model parameters might provide a better match to the observed atmospheric flux variations. However, such models do not fully capture the interplay of radiative, dynamical, and chemical processes in a planet’s atmosphere. Here we present new atmospheric models for HD 80606b that more fully explore the physical processes at work in HD 80606b’s atmosphere. Our models are three-dimensional (latitude, longitude, and pressure) and include full radiative transfer calculations that consider equilibrium chemistry processes in HD 80606b’s atmosphere throughout its highly eccentric orbit. We specifically explore how assumed rotation period plays a role in shaping global circulation patterns and how the formation and evolution of clouds might play a role in shaping the observed flux variation of HD 80606b. The following sections outline the specifics of our modelling approach, explore the complex atmospheric physics at work in HD 80606b, and provide observational predictions that give further insights into the current *Spitzer* observations and guide future atmospheric characterization observations of the HD 80606 system.

## 2. MODELS

The results presented here for our atmospheric modeling effort rely on a combination of simulation tools that link the physical processes potentially at work in HD 80606b’s atmosphere and what can be observed. In the following sections we present an overview of the global circulation, cloud, and observational phase curve models employed in this study.

### 2.1. Global circulation model

In the simulations presented here we employ the Substellar and Planetary Atmospheric Radiation and Circulation (SPARC) model first presented in Showman et al. (2009) as applied to HD 189733b and HD 209458b and subsequently used in a number of other exoplanet studies (e.g. Lewis et al. 2010; Kataria et al. 2013; Lewis et al. 2014; Kataria et al. 2014, 2015; Showman et al. 2015; Kataria et al. 2016; Parmentier et al. 2016). At the core of the SPARC model is the MITgcm (Adcroft et al. 2004), which solves the primitive equations with pressure as the vertical coordinate. We determine the amount of heating/cooling at each grid point by the divergence of radiative fluxes in each model layer. Radiative fluxes are calculated using the two-stream non-gray radiative transfer model of Marley & McKay (1999). We use the correlated-k method with 8 k-coefficients inside each of our 11 wavelength bins. These simulations of HD 80606b utilize the cubed-sphere grid (Adcroft et al. 2004) with a horizontal resolution of C16 ( $\sim 32 \times 64$  in latitude and longitude) and a vertical pressure range from 200 bar to 0.20 mbar broken down into 39 layers with even log-pressure spacing with a top layer that extends to zero pressure.

In the simulations presented here we assume an atmospheric composition of  $1 \times$  solar values and have excluded TiO and VO from the opacity tables since it is likely that these species are ‘cold trapped’ deep in the atmosphere (Fortney et al. 2008). Clouds are neglected in the global circulation model. The effect of clouds is, however, considered in the post-processing of the simulation. We define our planetary and stellar parameters using the values from Pont et al. (2009). The nominal rotation period of HD 80606b is determined to be 40.4761 hours assuming the pseudo-synchronous rotation relationship presented in Hut (1981). Because it is possible that HD 80606b’s rotation period might significantly deviate from this nominal value, we construct additional atmospheric models where the rotation period is assumed to be half (20.2380 hours) and twice (80.9522 hours) the nominal pseudo-synchronous rotation period. We initialize the model with wind speeds set to zero and each column of the grid assigned a pressure-temperature profile derived from one-dimensional radiative equilibrium calculations assuming that the planet is at periapse. The planet loses ‘memory’ of this initial temperature distribution fairly rapidly and we have found no significant difference between simulations started near periapse and those initialized near apoapse with the corresponding pressure-temperature profile.

We find that in order to maintain numeric stability near periapse that the timestep used to solve the relevant momentum and energy equations must be very short ( $\sim 5$  s). There is a high computational overhead associated with solving for our radiative fluxes along each grid column. We elect to update our radiative fluxes using a radiative timestep of 5 s near periapse, 20 s in the region 3.5 to 17.7 hours away from periapse, and 50 s for the remainder of the orbit to increase our computational efficiency. This radiative timestep scheme allows us to update the radiative fluxes in our model more frequently near periapse where the incident flux on the planet is changing rapidly and less frequently near apoapse where the relative change in the incident flux on the planet is smaller. We determine the time-varying incident flux on HD 80606b from its host star by calculating the planet-star distance at each radiative timestep using Kepler’s equation (Murray & Dermott 1999). We integrate our models for up to 1000 simulated days, but it is clear that the velocity profile for each orbit has reached a stable configuration after just a few orbits of the planet ( $\sim 300$  simulated days). Integrating our simulations beyond this point results in only small changes in planetary wind and thermal patterns that are confined to pressures well below photospheric pressures ( $\sim 300$  mbar).

### 2.2. Cloud modeling

As shown in Section 3, our global circulation model predicts that the dayside temperature of the planet can vary by more than 700 K between periapse and apoapse in the observable portion of the atmosphere. As such, the photospheric layers (1 bar to 1 mbar) can cross the condensation curves of several potential cloud species (e.g. Morley et al. 2012; Marley et al. 2013). To simulate the formation, dissipation and general evolution of clouds in HD 80606b’s atmosphere, we use the cloud model presented in Parmentier et al. (2016). In a given atmospheric column, a material is condensed if the temperature is cooler than its condensation temperature at a given pressure level in the atmospheric general

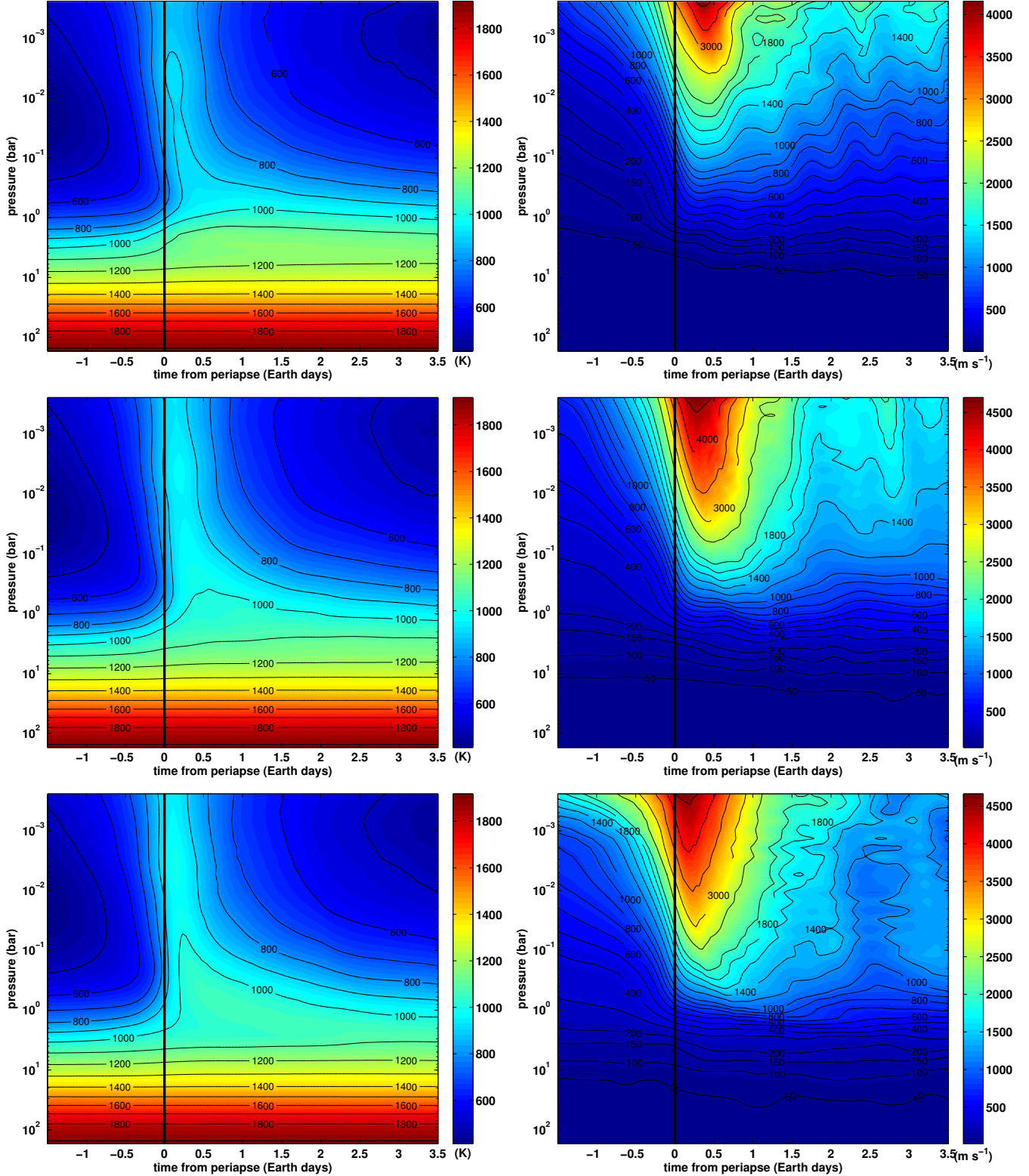


**Figure 1.** Average temperature (left) and RMS horizontal velocity (right) as a function of time relative to periapse passage for our half-nominal (top), nominal (middle), and twice-nominal (bottom) rotation period models. The temperatures and RMS velocities represent averages over latitude and longitude as a function of pressure.

circulation model. Clouds are assumed to condense with a uniform particle size of  $a$ , which is a free parameter ranging from  $0.1\mu\text{m}$  to  $10\mu\text{m}$ . In this study of HD 80606b, we consider the following possible cloud species:  $\text{MgSiO}_3$  (enstatite),  $\text{MnS}$  (manganese sulfide), and  $\text{Na}_2\text{S}$  (sodium sulfide). Cloud species  $\text{ZnS}$  and  $\text{KCl}$  are not considered in this study as they are fully evaporated from the planet's dayside during periastron passage and are expected to form

significantly less massive, and less opaque, clouds compared with  $\text{MgSiO}_3$ ,  $\text{MnS}$ , and  $\text{Na}_2\text{S}$  (e.g. Fortney 2005).

### 2.3. Theoretical Phase Curve Calculation

To calculate theoretical phase curves, planetary flux as a function of time, we solve the two-stream radiative transfer equations along the line of sight for each atmospheric column and for each planetary orbital position. In our radiative transfer calculations, we consider absorption, emission and scattering. This method, similar to the calculations of Fortney et al. (2006), naturally takes into account geometrical effects such as limb darkening and the variation of the stellar and planetary orientations with respect to each other and a earth-based observer. The stellar flux is assumed to be a collimated flux propagating in each atmospheric column with an angle equal to the angle between the local vertical and the direction of the star. We use 196 frequency bins ranging from 0.26 to 300  $\mu\text{m}$  and integrate the resulting outgoing flux over a variety of observational bandpasses spanning the visible to infrared wavelengths (0.3-28  $\mu\text{m}$ ). The gaseous opacities used to calculate the values of the k-coefficients are the same as the ones used for the global circulation model calculations. Rayleigh scattering by the gas and Mie scattering by the clouds are combined with the gaseous opacities to produce our theoretical spectra as a function of time for HD 80606b.

In this study, cloud opacities are included in post-processing and not self-consistently included within the framework of the global circulation model. This is done to maintain the computational feasibility of our atmospheric models. A single SPARC model can require weeks to months of computational time in a cluster computing environment to reach a stable solution, largely limited by computational requirements of the fully non-gray radiative transfer calculations. Incorporation of cloud formation, evolution, and radiative feedback is not impossible within the framework of the SPARC model, but would currently require prohibitively long computation times. As shown by (Parmentier et al. 2016), the cloud distribution in hot Jupiters is primarily determined by the thermal structure of the planet, with radiative feedback and the dynamical mixing of the clouds being secondary effects. Therefore, the cloud distributions we derive here from our models should be a good approximation for the spatial and wavelength dependent opacities we could expect to shape HD 80606b's phase curve. We are currently working on further optimization to the SPARC and cloud formation models to more robustly treat clouds without requiring highly tuned or parameterized schemes.

## 3. RESULTS

The following sections overview the key results from our atmospheric modelling effort for HD 80606b. We first present changes in the global scale winds and temperatures of HD 80606b as a function of both pressure and time for our half-nominal, nominal, and twice-nominal rotation period models. We then compare the thermal patterns and winds predicted for HD 80606b near the periapse and apoapse of its orbit from our half-nominal, nominal, and twice-nominal rotation period atmospheric models. We further focus on the thermal structure and vertical wind profiles as a function of longitude that develop in our models near periapse. Using the post-processing method described in Section 2.2, we predict the evolution of cloud coverage in HD 80606b. Finally, we present theoretical phase curves derived from our simulations for each rotational period case assuming a range of cloud properties and compare them with the *Spitzer* observations at 4.5 and 8  $\mu\text{m}$  presented in de Wit et al. (2016).

### 3.1. Global Scale Winds and Temperatures

Since our simulations are performed in three-dimensions, we can investigate changes in the overall temperatures and wind speeds of HD 80606b as a function of depth in the atmosphere as well as time. Figure 1 presents globally averaged temperatures and root mean square (RMS) horizontal velocities as a function of pressure and time relative to the periapse of HD 80606b's orbit for each of our rotation period cases. The peak global average atmospheric temperatures near the 340 mbar level in our simulations occurs on average 11 hours after periapse passage. Near the 10 mbar level of our simulation where radiative timescales are shorter, peak temperatures are reached on average 4.5 hours after periapse passage. In all cases peak wind speeds are achieved  $\sim 2$  hours after the peak in the planetary temperature. It is also interesting to note that both temperatures and wind speeds remain elevated with respect to their pre-periapse values for several days to weeks depending on the pressure level for all of our models regardless of the assumed rotation period (Figure 1). HD 80606b transits its host star as seen from earth  $\sim 5.6$  days after periapse passage (Moutou et al. 2009), so these elevated temperatures and wind speeds could be relevant to transit observations of this planet.

Because HD 80606b is subject to large variations in the amount of flux it receives from its host star it is likely to show distinct changes in wind and thermal patterns as a function of orbital phase. Figure 2 shows the zonal-mean zonal winds for HD 80606b near the apoapse and periapse of its orbit for each of our rotation period cases. The term zonal wind refers to the component of the wind vector that is in the east-west direction while the zonal mean is an average over all longitude for a given latitude. For most its orbit, HD 80606b maintains a fairly steady jet structure similar to the apoapse jet structures presented in the right half of Figure 2. The width and number of jets that develop in our simulations of HD 80606b near the apoapse of its orbit is dependent to a large degree on the assumed rotation period of the planet (Showman & Guillot 2002; Showman et al. 2008, 2010, 2015). As HD 80606b approaches the periapse of its orbit, its jet structure dramatically changes. At low pressures in all of our rotation period cases strong westward flows develop as air rushes from the day to the night side of the planet. In our nominal and twice-nominal rotation period cases, predominately eastward flow is maintained at pressures higher than  $\sim 10$  mbar. In the half-nominal rotation period case, the high latitude eastward jets are maintained through out the orbit, strengthening and weakening with the amount of incident flux on the planet.

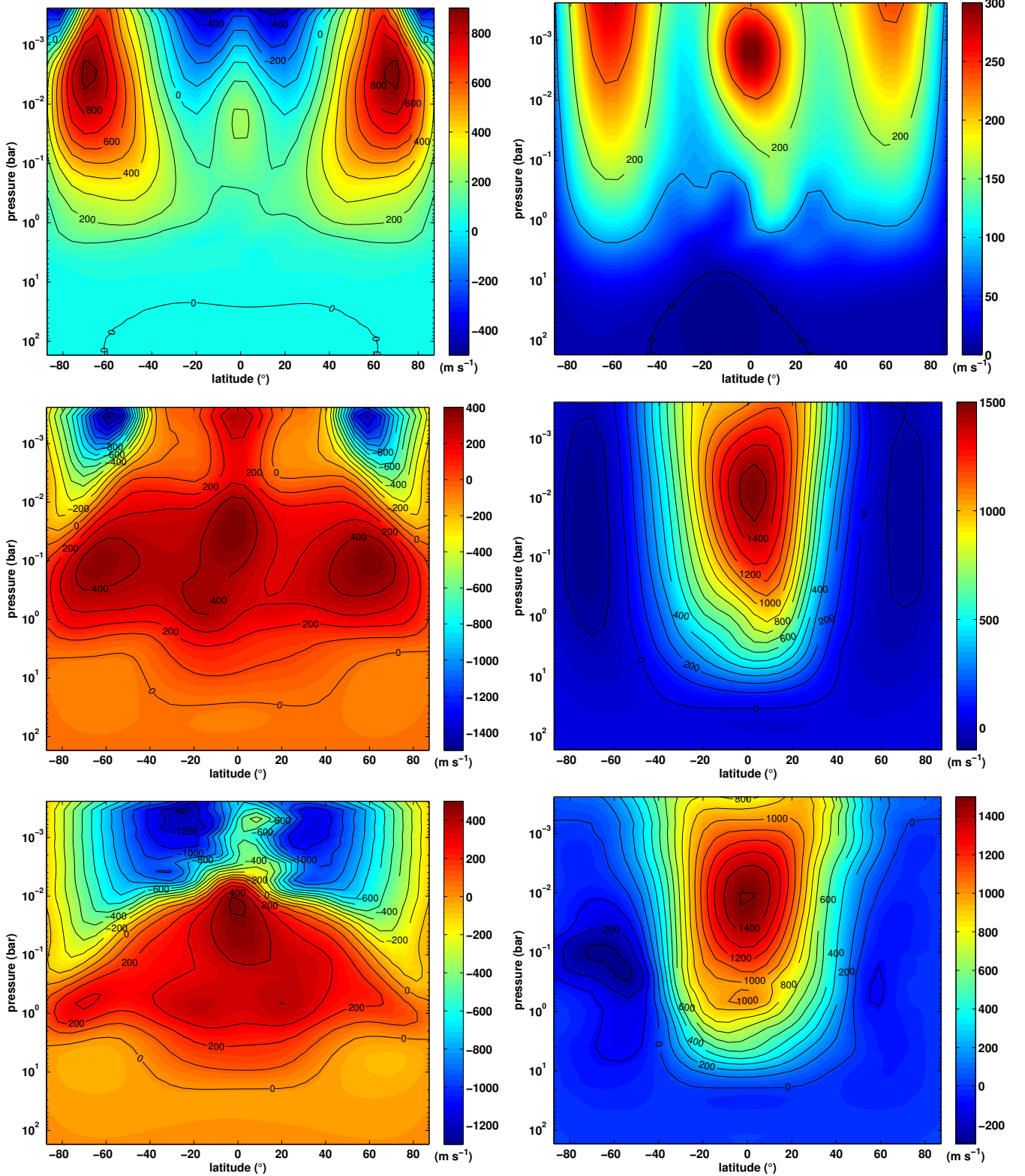


**Figure 2.** Zonal-mean zonal winds for HD 80606b near periape (left) and apoapse (right) for our models that assume the half-nominal (top), nominal (middle), and twice-nominal (bottom) rotation period for the planet. Apoapse and periape occur at true anomalies ( $f$ ) of  $180^\circ$  and  $0^\circ$  respectively. The colorbar shows the strength of the zonally averaged winds in  $\text{m s}^{-1}$ . Contours are spaced by  $100 \text{ m s}^{-1}$ . Positive wind speeds are eastward, while negative wind speeds are westward. Note the significant change in the jet structure as a function of orbital position.

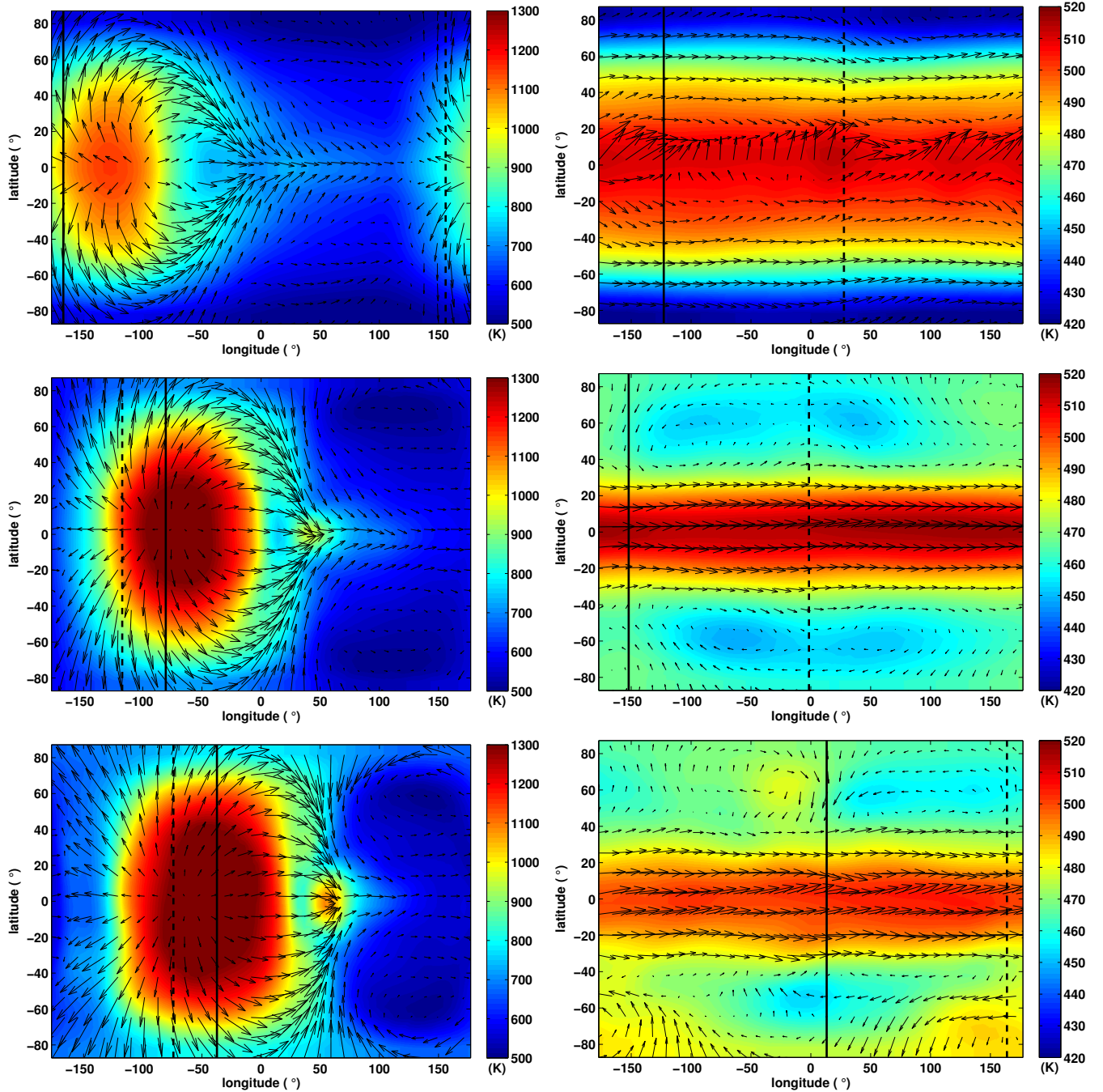


**Figure 3.** Temperature (colorscale) and horizontal winds (arrows) at the 340 mbar level of our HD 80606b model near periape (left) and apoapse (right) for our half-nominal (top), nominal (middle), and twice-nominal (bottom) rotation period cases. The length of the arrows represent the strength of horizontal winds. The longitude of the substellar point is indicated by the solid vertical line. The Earth facing longitude is indicated by the dashed vertical line.

The rapid heating that HD 80606b experiences as it passes through periape results not only in changes in the planet’s jet structure, but also produces significant changes in its horizontal temperature distribution. Figure 3 shows the temperature distribution and wind vectors at the 340 mbar level of our simulations near the periape and apoapse of HD 80606b’s orbit. Near apoapse, HD 80606b’s atmospheric temperature distribution at the 340 mbar level of our simulations is fairly uniform with longitude but shows an equator to pole temperature difference that increases with decreasing rotation period. The efficiency of equator to pole heat transport is strongly influenced by the assumed rotation period of the planet. The larger latitudinal gradient in temperature in our half-nominal rotation period case results from the fact that equator to pole heat transport becomes less efficient as the rotation period is reduced (e.g., Showman et al. 2015).

Near the periape of its orbit, the temperature distribution of HD 80606b becomes dominated by a strong day-night temperature contrast (Figure 3). The strength of this day-night temperature contrast is determined in part by the

path travelled by the longitude of the substellar point as determined by a combination of the orbital geometry and the rotation period of the planet. In our nominal rotation period case, the longitude of the substellar point ( $\phi_*(t)$ ) becomes stationary near periapse and the heating becomes confined to the region near that longitude. For our half-nominal rotation period case, the time rate of change of  $\phi_*$  slows, but continues in a westward motion heating other longitudes and muting the day/night temperature contrast. In our twice-nominal rotation period case,  $\phi_*(t)$  changes in an eastward motion near periapse, revisiting previously heated regions of the atmosphere and increasing the width of the hot spot on the dayside. This, in turn, affects the magnitude of the day-night temperature contrast and also the efficiency of day-night versus equatorial flow. In all of our rotation period cases, we see some convergence of the flow from the planet’s dayside in the region between the eastern terminator and the nightside of the planet (left side of Figure 3).

The orientation of HD 80606b’s orbit ( $e = 0.93$  and  $\omega = 300.80^\circ$ , Pont et al. (2009)) is such that secondary eclipse, when the planet passes behind the host star as seen from Earth, occurs just three hours before periastron passage. This is an observationally advantageous orbital configuration for studies of planetary atmospheric response near periapse passage and has been leveraged in the phase-curve studies of Laughlin et al. (2009) and de Wit et al. (2016). Phase-curve observations largely probe longitudinal brightness variations (Cowan & Agol 2008), which in the case of HD 80606b vary strongly as a function of time. Figure 4 shows the latitude-weighted average temperature as a function of longitude from substellar point and pressure that evolves in our models of HD 80606b near periapse and apoapse. Near apoapse, our atmospheric models show virtually no variation in temperature from the planet’s dayside to nightside, with temperatures ranging from  $\sim 400$ -600 K above 1 bar. Near periapse, however, our atmospheric models of HD 80606b manifest large ( $\sim 500$  K above 10 bar) temperature variations with longitude. The longitudinal location the peak temperatures and the depth to which the thermal structure of the planet is altered during periapse passage is a function of the assumed rotation period (Figure 4). The offset of peak temperatures away from the substellar point increases with decreasing rotation period of the planet as the strength of the day-night vs equatorial flow decreases. Similarly, the depth to which the planet’s thermal structure is significantly altered increases with increasing rotation period, which reflects the duration that particular longitudes are exposed to incoming stellar radiation during periapse passage.

The transport of cloud material in HD 80606b’s atmosphere near periapse passage will depend critically on both horizontal (see Figures 2 and 3) and vertical transport in the planet’s atmosphere. Figure 5 shows the latitude-weighted average vertical wind as function of longitude from the substellar point and pressure in our HD 80606b models near periapse and apoapse. Near apoapse, vertical velocities in our HD 80606b models are fairly weak ( $\sim 0.05$  m s $^{-1}$ ), with patterns of updrafts and downdrafts that vary based on the assumed rotation period of the planet. Near periapse, strong updrafts develop on the dayside and strong downdrafts on the nightside of the planet in our models of HD 80606b’s atmosphere. These regions of updrafts and downdrafts near periapse correspond to regions of horizontal wind divergence and convergence seen in Figure 3. The location and depth of the strongest regions of updrafts and downdrafts vary with assumed rotation period, with the twice-nominal rotation period model manifesting the deepest updraft that is mostly closely located near the substellar longitude. Under all rotation period assumptions, the presence of strong dayside updrafts could allow for cloud material located at depth in HD 80606b’s atmosphere to be lofted into the visible regions of the planet’s atmosphere.

### 3.2. Cloud Formation and Evolution

Rapid formation/dissipation and transport of clouds is likely to occur in the atmosphere of HD 80606b during periapse passage. As shown in Figure 6 the evolution of the cloud coverage through periapse passage depends on the cloud species’ condensation temperatures. When HD 80606b’s atmospheric temperatures do not exceed the cloud condensation temperature, such as for MgSiO $_3$  or MnS clouds, the planet is fully cloudy all the time. When the atmospheric temperatures get hotter than the condensation temperature, such as for Na $_2$ S clouds, then a hole in the clouds forms when the planet gets close to periapse (see Figure 4), qualitatively affecting the flux maps shown in Figure 6. By measuring the evolution of the cloud coverage in HD 80606b, one could possibly determine the most probable cloud composition. For all cloud compositions considered in this study, the nightside should remain cloudy during periapse passage, leading to a dimming of the atmosphere at infrared wavelengths.

Atmospheric transport of cloud particles, not self-consistently considered here, could affect the picture presented in Figure 6. At apoapse, all the clouds modeled here have cloud bases well below the photosphere near 300 mbar. If vertical mixing is small, then these species are trapped near the cloud base and should not be present in the observable portion of the atmosphere. During periapse, strong updrafts on the dayside can transport the cloud material from its original cloud base to the observable atmosphere (see Figure 5). Horizontal winds can also potentially play a role in transporting material lofted on the dayside to the nightside of the planet (see Figures 2 and 3).

The depth of the cloud bases near apoapse strongly depends on the under-constrained internal temperature profile of HD 80606b. Tidal dissipation (e.g. Bodenheimer et al. 2001) and other atmospheric processes (e.g. Ohmic dissipation, Batygin & Stevenson (2010)) could significantly increase the deep temperature profile of HD 80606b and raise the cloud deck closer to the photosphere. In our models we have assumed an internal temperature ( $T_{\text{int}}$ ) of 100 K, which is consistent with the internal temperature of Jupiter (Fortney et al. 2011). If the assumed internal temperature of HD 80606b was raised to 500 K or 1000 K the temperature at 200 bar level in our model atmospheres would be increased to roughly 3000 K and 4000 K respectively. This increase in the internal temperature would cause an ‘upward’ shift in the thermal structure of the models presented in Figure 4, which would result in the cloud base pressure for MgSiO $_3$  to move from roughly 100 bars to 10 bars and 1 bar under the assumption that  $T_{\text{int}}$  equals 500 K

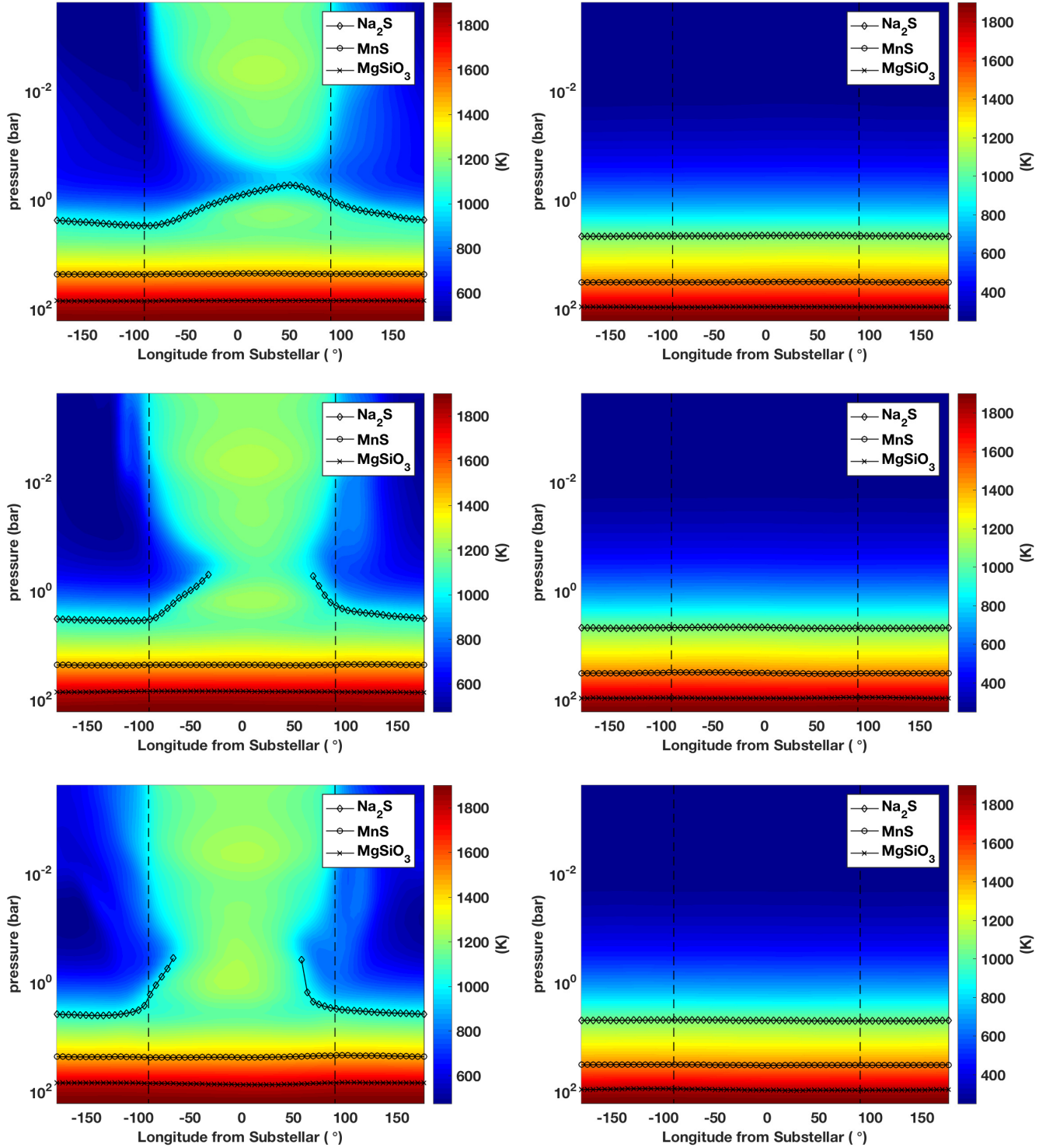


**Figure 4.** Temperature (colorscale) averaged in latitude as a function of pressure and degrees from the substellar longitude near periapse (left) and apoapse (right) for our half-nominal (top), nominal (middle), and twice-nominal (bottom) rotation period cases near periapse. Temperatures represent average values weighted by  $\cos \phi$ , where  $\phi$  is latitude. Contours in panels represent condensation points, in pressure-temperature space, for the cloud species considered in this study. Note the thermal inversion that develops at pressure less than 1 bar near periapse.



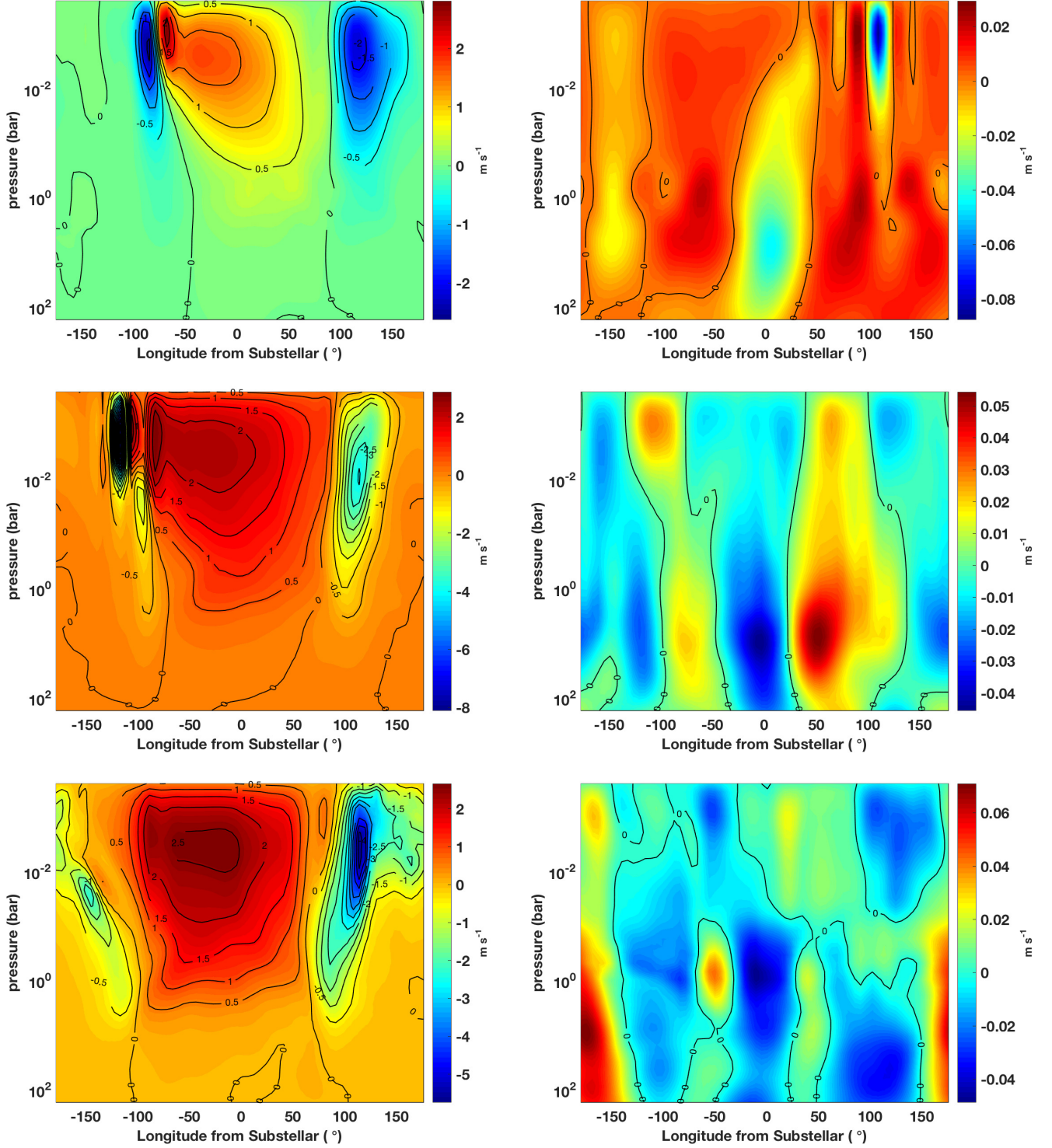


**Figure 5.** Vertical velocity averaged in latitude as a function of pressure and degrees from the substellar longitude near periapse (left) and apoapse (right) for our half-nominal (top), nominal (middle), and twice-nominal (bottom) rotation period cases. Vertical velocities represent average values weighted by  $\cos \phi$ , where  $\phi$  is latitude. Positive vertical velocity values represent updrafts while negative vertical velocities represent downdrafts. Note the significant updrafts that develop on the dayside of HD 80606b in our models near periapse passage.

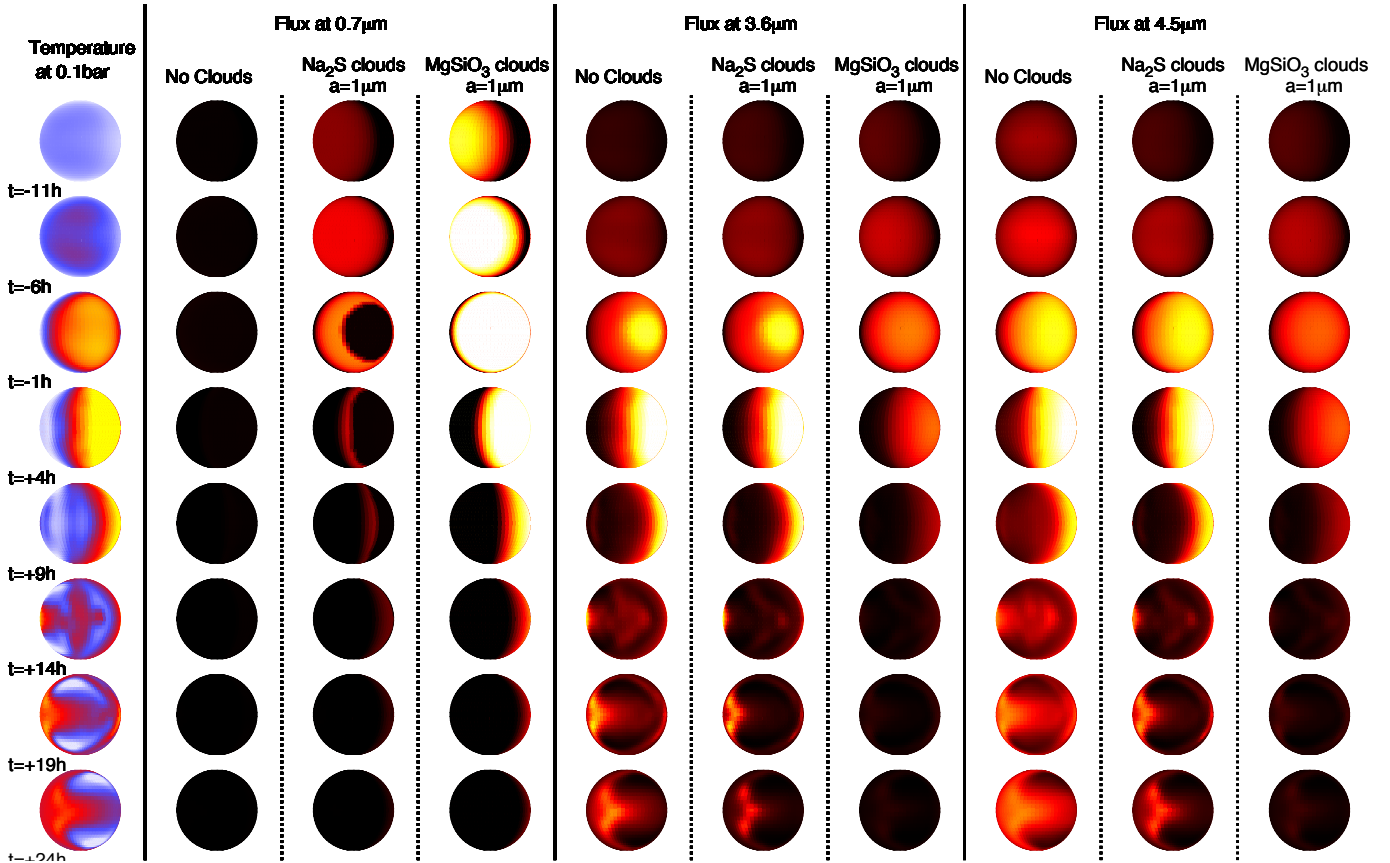


**Figure 6.** Temperature at 0.1bar (left column) and flux emerging from the Earth-facing planet hemisphere at three different wavelengths assuming either that the atmosphere is cloudless or that  $\text{Na}_2\text{S}$  or  $\text{MgSiO}_3$  clouds are present. The different rows are for different times, with  $t = 0$  being the periape passage. The temperature scale ranges linearly from 500K to 1200K. The brightness scale is linear and normalized for each wavelengths to the brightest point simulated, so brightness maps can be compared between different times and different cloud species but not between different wavelengths. At  $0.7\mu\text{m}$  the planetary flux is dominated by reflected light and cloudy parts appear bright and cloudless parts appear dark. At longer wavelengths, dominated by thermal emission, the presence of clouds raises the photosphere to higher, cooler layers and the planet appears dimmer.  $\text{Na}_2\text{S}$  clouds disappear partially from the dayside at  $t = -1\text{h}$  when the planet becomes hotter than the condensation temperature. On the contrary,  $\text{MgSiO}_3$  clouds are always present.

and 1000 K, respectively.

During periape passage, an updraft with a vertical velocity of on average  $1\text{ m s}^{-1}$  develops on the dayside of our HD 80606b atmospheric models that persists for  $\sim 1$  day (Figure 7). This dayside updraft can lift particles over  $\sim 100$  km in atmospheric height, corresponding to two scale heights and thus one order of magnitude in pressure. As a consequence, only particles from pressures shallower than  $\sim 3$  bars can be lofted above the photosphere during periape to form an observable cloud. If we assume that at apoapse the cloud layers are approximately one scale height thick, then only clouds that have a cloud base pressures shallower than  $\sim 10$  bar can be present in the observable portion of HD 80606b’s atmosphere. In the case of a cool deep temperature profile ( $T_{\text{int}}=100\text{ K}$ ), only  $\text{Na}_2\text{S}$  clouds can be lofted above the photosphere during periape passage. If deep atmosphere is hotter ( $T_{\text{int}}=500\text{ K}$ ), then  $\text{MgSiO}_3$  and  $\text{MnS}$  clouds could also be present. Observational determination of the composition of clouds present in HD 80606b’s atmosphere during periape passage could help constrain the deep pressure temperature profile of the planet.

### 3.3. Theoretical Light Curves

The SPARC model is uniquely equipped to produce theoretical light curves and spectra for HD 80606b that account for spatial thermal variations, cloud coverage and dynamics within the atmosphere (see Fortney et al. 2006; Showman et al. 2009). This capability allows us to make observational predictions based on a variety of assumptions about the planet’s atmospheric composition (in this case clouds) and rotation period. In this section, we focus our model-observation comparisons on the *Spitzer* 4.5 and  $8\mu\text{m}$  bandpasses used in de Wit et al. (2016) to study HD 80606b. We consider both cloud-free and cloudy models when exploring derived theoretical phase curves and comparing them with the phase variations observed for HD 80606b near periape.

#### 3.3.1. Model-Observation Comparisons: Cloud-Free

Given the potential for clouds to be sequestered well below the photosphere of HD 80606b or rapidly dissipated near periastron passage (see Figures 4), it is possible that clouds play a negligible role in shaping HD 80606b’s time-varying flux. Figure 8 presents theoretical light curves at *Spitzer*’s 4.5 and  $8\mu\text{m}$  assuming the half-nominal, nominal and

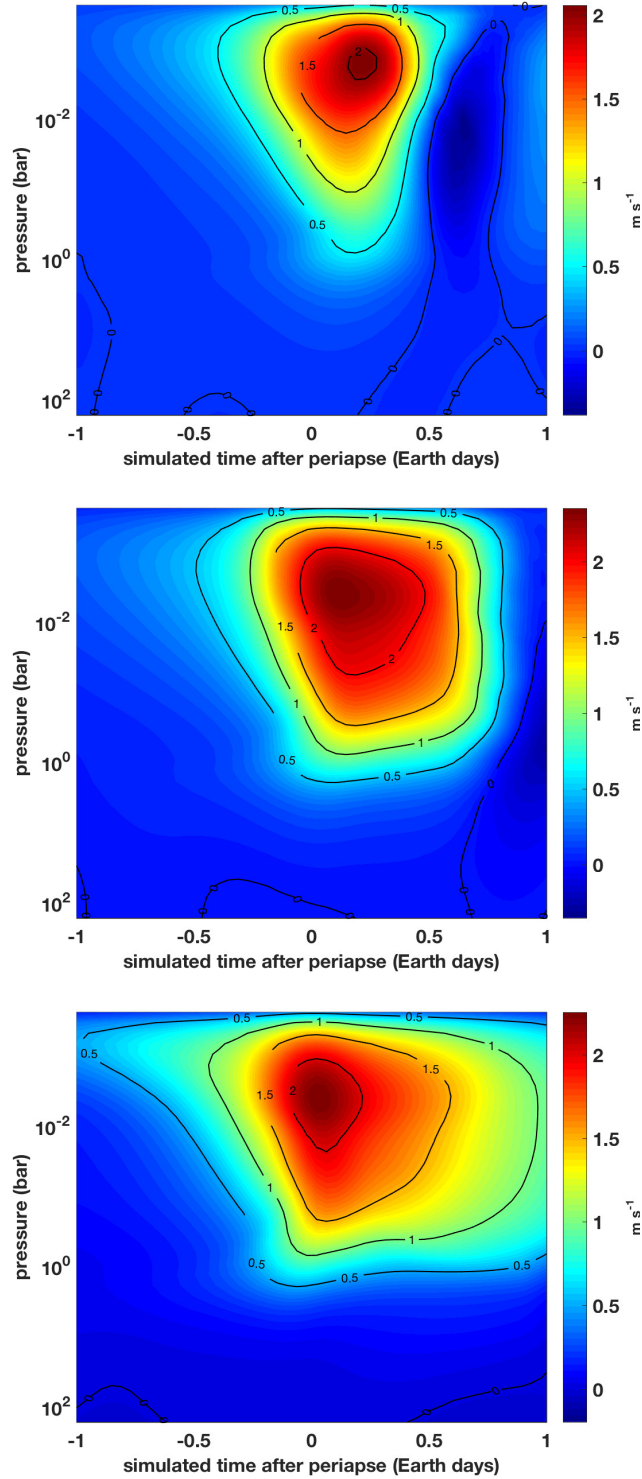


**Figure 7.** Dayside average vertical velocity ( $\text{m s}^{-1}$ ) as a function of pressure and time from periape passage for our half-nominal (top), nominal (middle), and twice-nominal (bottom) rotation period cases. Positive vertical velocity values represent updrafts while negative vertical velocities represent downdrafts. The strong updraft that develops in the dayside of our HD 80606b models near periape persists in the atmosphere for  $\sim 1$  day. Note that the strength and duration of the dayside updraft depends on the rotation period assumed for the planet.

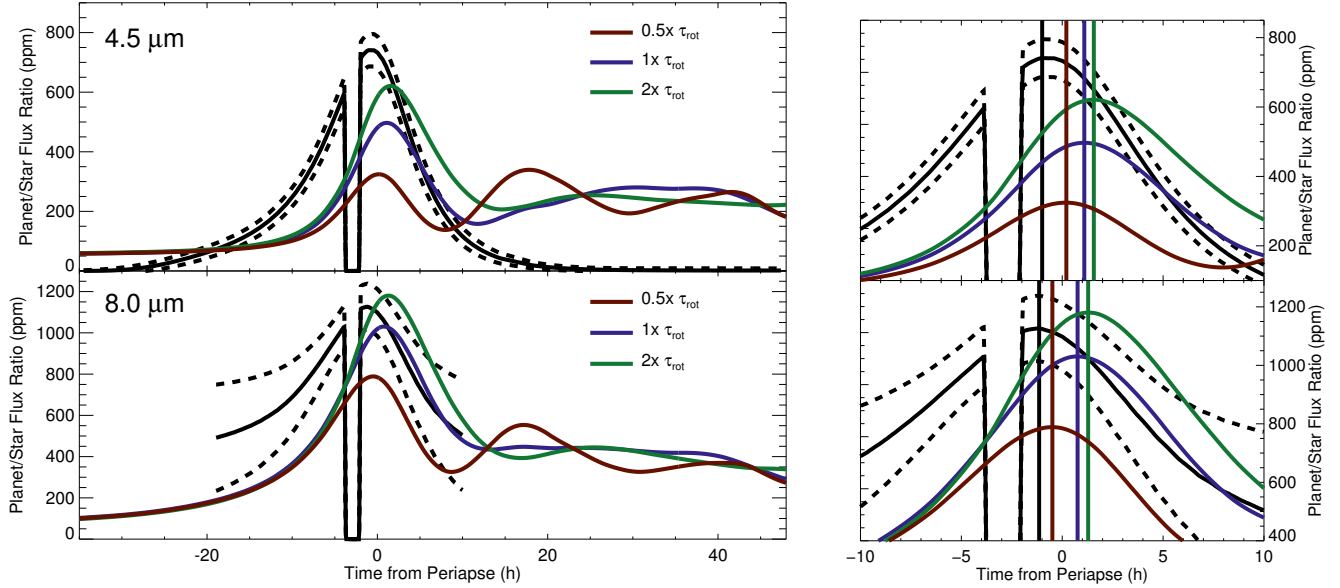


**Figure 8.** Observed Planet/Star flux ratio (in parts per million, ppm) as a function of time from periapse passage in the *Spitzer* 4.5 and 8.0  $\mu\text{m}$  channels presented in de Wit et al. (2016). Dashed lines represent the  $1\sigma$  envelopes for the observed phase variations. Theoretical phase curves derived from the half-nominal (red), nominal (blue), and twice-nominal (green) rotation period cloud-free models of HD 80606b presented in this study are included for comparison. Right panel is a zoom-in of the left panel in the region near periapse passage. Vertical lines in right panel represent location of the peak of the planetary flux. Note that all of our cloud-free models over-predict the time of flux maximum. The twice-nominal (green) model provide the best match of the observed phase amplitude, which is consistent with the rotation period derived by de Wit et al. (2016).

twice-nominal rotation period for the planet. The amplitude and shape of the light curves near periapse passage is a strong function of the assumed rotation period. The orbital configuration of HD 80606b is such that an earth observer sees the full dayside hemisphere three hours before the periapse passage. As HD 80606b continues to rotate, more and more of the nightside hemisphere contributes to the observable flux from the planet. We find that peak of the observable planetary flux from our HD 80606b models peaks very near periapse as the result of the combination of planetary rotation period, radiative timescales, and observing geometry of the system.

The timing of the predicted peak of the planetary flux does vary with the assumed planetary rotation period and the observational bandpass being considered. In the 8  $\mu\text{m}$  bandpass, our models predict the timing of the peak observable planetary flux to occur 0.5 hours before, 0.75 hours after, and 1.3 hours after periapse passage for the half-nominal, nominal, and twice-nominal rotation periods respectively. In the 4.5  $\mu\text{m}$  bandpass, our models predict the timing of the peak observable planetary flux to occur 0.2, 1.1, and 1.6 hours after periapse passage for the half-nominal, nominal, and twice-nominal rotation periods respectively. In all cases, our models over-predict the time of peak observable flux for HD 80606b compared with the  $\sim 1$  hour before periapse passage observed by de Wit et al. (2016) in both the 4.5 and 8.0  $\mu\text{m}$  channels.

We also find that the magnitude of the peak of the planetary flux is a strong function of the assumed rotation period. This is not surprising since the rotation period of the planet determines both the rate at which the substellar point sweeps in longitude, but also the fraction of the dayside hemisphere viewed by an earth observer. We find peak values in the planet/star flux ratio at 8  $\mu\text{m}$  of 790 ppm, 1030 ppm, and 1180 ppm for the half-nominal, nominal, and twice-nominal rotation period cases respectively compared with the observed peak value of 1130 ppm from de Wit et al. (2016). We find peak values in the planet/star flux ratio at 4.5  $\mu\text{m}$  of 320 ppm, 500 ppm, and 620 ppm for the half-nominal, nominal, and twice-nominal rotation period cases respectively compared with the observed peak value of 740 ppm from de Wit et al. (2016). The twice-nominal rotation period model for HD 80606b provides the best match to the amplitude of the observed flux variation presented by de Wit et al. (2016).

In addition to the peak in the planetary flux near periapse, we find that in each of our rotation cases secondary peaks in planetary flux occur. For our half-nominal rotation case, the peaks occurs on an interval approximately equal to the assumed rotation period of 20.2380 hours. The second peak in the half-nominal rotation period case, occurs slightly before 20.2380 hours from the first peak, which is a result of the sub-Earth longitude probing the remnants of a compressional heating event. The secondary peaks in the nominal and twice-nominal rotation period cases occur between one and two days after periapse passages are also the result of the sub-Earth longitude crossing the longitude region affected by a compressional heating event in each case. The observed phase variations of HD 80606b do not exhibit the predicted ‘ringing’ (Cowan & Agol 2011; Kataria et al. 2013), which was cited by de Wit et al. (2016) as further support for the exceptionally long planetary rotation period inferred from the observational data ( $\sim 93$  hours).

### 3.3.2. Model-Observation Comparisons: Cloudy

Longer Rotation Period  $\longrightarrow$

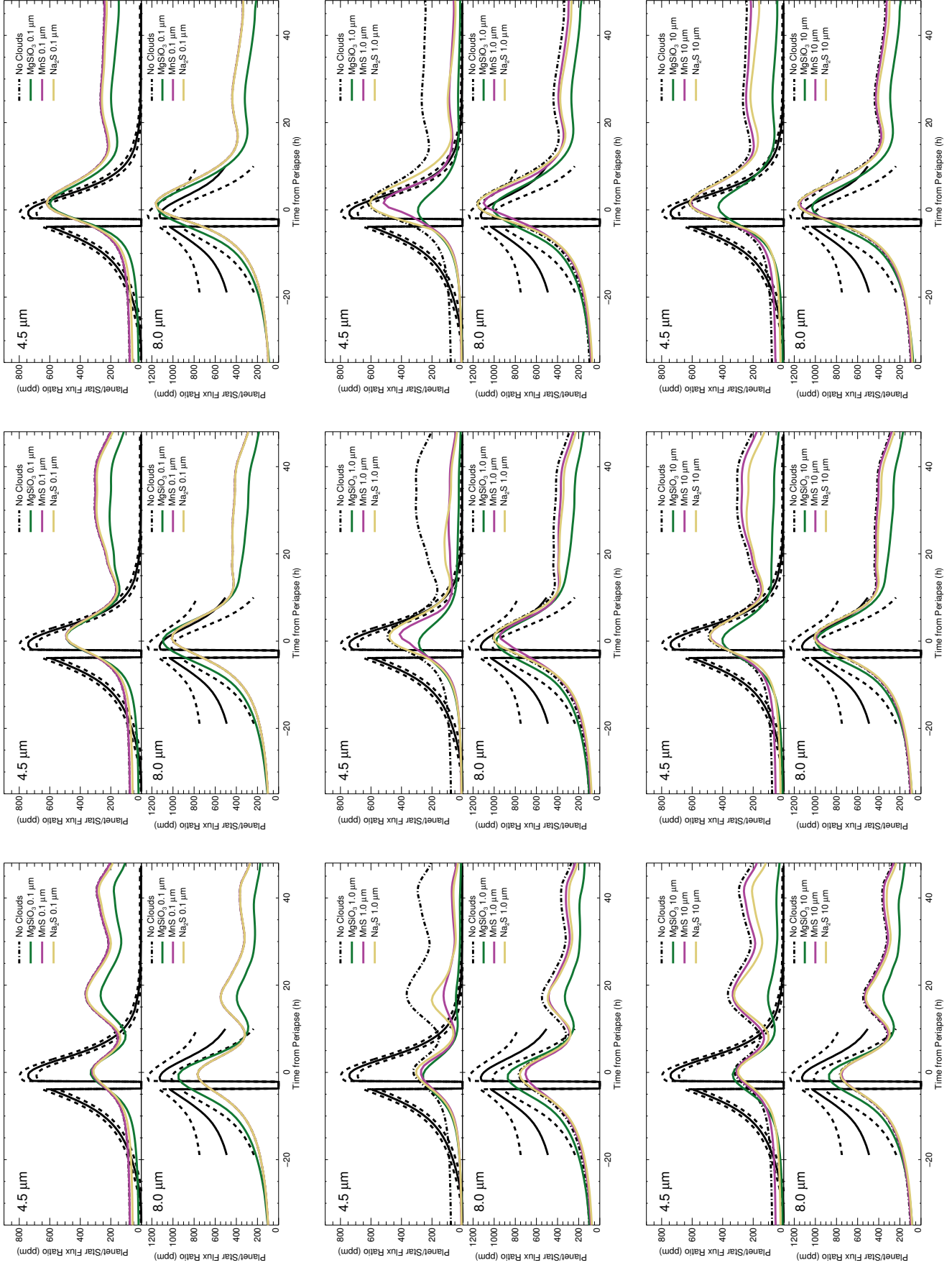


**Figure 9.** Planet/Star flux ratio (in parts per million, ppm) as a function of time from periape passage as observed with *Spitzer* (solid black lines with dashed black line  $1\sigma$  envelopes) and as predicted from our models with half-nominal (left panels), nominal (middle panels), and twice-nominal (right panels)  $\text{MgSiO}_3$  (green), MnS (magenta), and  $\text{Na}_2\text{S}$  (yellow) clouds with particle sizes of  $0.1\ \mu\text{m}$  (top panels),  $1.0\ \mu\text{m}$  (middle panels),  $10\ \mu\text{m}$  (bottom panels). Accounting for the presence of clouds does improve the consistency of the model phase curve predictions with the *Spitzer* observation in the regions away from periape passage.

It is possible that clouds will form in or be lofted into the photospheric regions of HD 80606b’s atmosphere during periapse passage (see Section 3.2). Figure 9 compares phase variations predicted using our models assuming a range of condensate species and particle sizes (see discussion in Section 2.2). We find that in the  $8\ \mu\text{m}$  bandpass assumed particle size ( $0.1\text{--}10\ \mu\text{m}$ ) does not significantly change the phase curve predictions for a given cloud species, but in all cases the presence of  $\text{MgSiO}_3$  clouds better suppresses the flux in region outside of periapse passage. A range of both cloudy and cloud-free models produce theoretical phase curves that are consistent with the  $8\ \mu\text{m}$  data given the uncertainties on the observed flux variations for HD 80606b at that wavelength. The  $8\ \mu\text{m}$  data are best matched by models that assume either the nominal or twice-nominal rotation period for the planet, consistent with the rotation period of the planet estimated by de Wit et al. (2016) ( $93 \pm_{35}^{85}$  hours).

The half-nominal rotation period model, while inconsistent with observations, does highlight a potentially interesting atmospheric effect that is lacking from our other models. In the half-nominal rotation period model, the presence of  $\text{MnS}$  or  $\text{Na}_2\text{S}$  clouds suppresses the flux near periapse passage while the presence of  $\text{MgSiO}_3$  clouds actually enhances the planetary flux near  $8\ \mu\text{m}$ . This increase in the peak planetary flux when including  $\text{MgSiO}_3$  clouds for the half-nominal rotation period model, as well as the nominal rotation period model with  $0.1\ \mu\text{m}$  size  $\text{MgSiO}_3$  cloud particles, occurs because the significant increase in atmospheric opacity causes the  $8\ \mu\text{m}$  photosphere to be pushed to shallower pressures that are dominated by the thermal inversion seen in the left panels of Figure 4. In general, the presence of  $\text{MgSiO}_3$  clouds tends to cause the predicted peak in the planetary flux to occur earlier than the cloud-free and  $\text{MnS}$  or  $\text{Na}_2\text{S}$  cloud models. This behavior in the peak flux timing can also be attributed to enhanced opacity causing shallower pressures, with shorter radiative timescales, to be probed.

Much like with the cloud-free cases (Figure 8), the model predictions for HD 80606b’s phase variations are not able to reproduce the observed flux variations at  $4.5\ \mu\text{m}$ . However, a few key trends can be noted that move us toward understanding the atmospheric processes shaping the *Spitzer*  $4.5\ \mu\text{m}$  observation. First, as postulated in de Wit et al. (2016), clouds are necessarily to suppress the flux from the planet in the regions outside of periapse passage. Second, the assumed average particle size of a particular cloud species does play a role in the predicted phase-curves behaviors at  $4.5\ \mu\text{m}$ , especially for  $\text{MgSiO}_3$  clouds. Overall, The twice-nominal rotation model including clouds, in particular  $1\ \mu\text{m}$  particle size  $\text{Na}_2\text{S}$  clouds, best reproduce the observed HD 80606b phase variations at  $4.5\ \mu\text{m}$ . The complexities of cloud formation and evolution are not fully captured by our current models, but our results indicate that aerosols play a significant role in shaping the flux variations observed by *Spitzer* for HD 80606b.

#### 4. DISCUSSION

Our three-dimensional general circulation models of HD 80606b provide for self-consistent treatment of a number of complex atmospheric processes without requiring model tuning and/or parametric schemes (e.g. Langton & Laughlin 2008; Cowan & Agol 2011). However, the complexity of our models does require detailed analysis of the circulation patterns, thermo-chemical structure, and cloud coverage that evolves, as we’ve performed in the previous sections. Here we discuss the key atmospheric physical processes that manifest in our models of HD 80606b that likely play a significant role in shaping the observed flux variation of HD 80606b near the periapse of its orbit.

Two scenarios currently exist to explain the lack of thermal emission from HD 80606b outside of periapse passage in the  $4.5\ \mu\text{m}$  *Spitzer* observations presented in de Wit et al. (2016). The first scenario is that the visible part of HD 80606b lacks clouds, because they could potentially be confined to depths well below the photosphere, and also does not have a significant internal luminosity. The second scenario is that HD 80606b has a significant internal luminosity, potentially due to tidal heating, and optically thick clouds impeding the internal heat flux to escape at the observed wavelengths. Our cloud-free models have a very small internal luminosity ( $T_{\text{int}} = 100\ \text{K}$ ), yet still predict a significant flux from HD 80606b post periapse passage inconsistent with the observations. Our cloudy models with optically thick  $\text{MgSiO}_3$  clouds provide the best method for suppressing the planetary flux outside periapse. Although none of our models can provide a ‘perfect’ fit to current observations, the most plausible scenario for HD 80606b is that an optically thick cloud deck is formed via lofting material from depth during periapse passage.

In de Wit et al. (2016), the lack of any visible atmospheric ‘ringing’ (Cowan & Agol 2011; Kataria et al. 2013) combined with the width of planetary flux ‘bump’ was used to constrain HD 80606b’s rotation period to be significantly longer than the pseudo-synchronous rotation period. As we’ve described here, the lack of atmosphere ‘ringing’ could in fact simply be due to the development of an optically thick cloud deck post periapse passage. However, we find that our models that assume twice the pseudo-synchronous rotation period still provide the best explanation of the width and amplitude of the flux variations of HD 80606b near periapse. Our models both with and without clouds over-predict the time of peak planetary flux relative to periapse. We see better alignment between the observed and predicted timing of the peak in planetary flux when a significant opacity source, such as  $\text{MgSiO}_3$  clouds, results in shallower pressures, with shorter radiative timescales, being probed by a given observational wavelength. In our cloud-free models, the radiative timescale we measure near the  $4.5$  and  $8.0\ \mu\text{m}$  photospheres ( $\sim 100\text{--}400\ \text{mbar}$ ) is  $\sim 8\text{--}12$  hours, which is longer than the  $\sim 4$  hour radiative timescale measured for HD 80606b by Laughlin et al. (2009); de Wit et al. (2016). The inclusion of  $\text{MgSiO}_3$  clouds in our models for HD 80606b raise the  $4.5$  and  $8.0\ \mu\text{m}$  photospheres to closer to  $10\ \text{mbar}$ , where the radiative timescales we measure in our models are more consistent with the observed values. It is likely that the pressures we’re probing in generating our synthetic phase curves are too deep in the atmosphere, which could be compensated for through enhanced opacity from aerosols, a more metal-rich atmosphere, and/or a strengthening of the thermal inversion that develops in the upper levels of our HD 80606b models (Figure 4).

##### 4.1. Observational Probes Beyond *Spitzer*

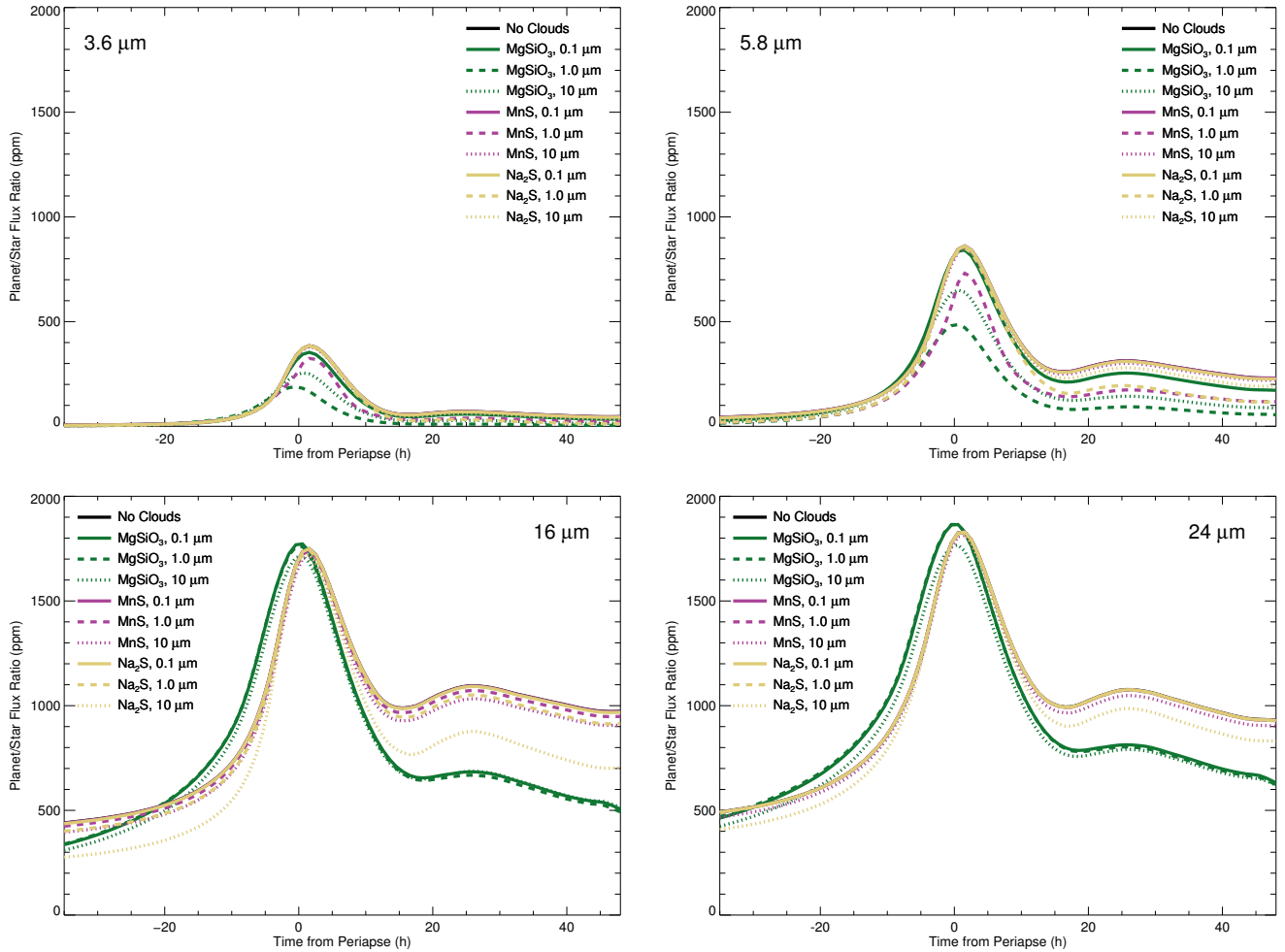


**Figure 10.** Theoretical Planet/Star flux variations for HD 80606b derived from our twice-nominal rotation period model assuming a range of cloud species and particle sizes for a range of *Spitzer* bandpasses. These wavelengths will also be accessible to JWST.

Observations at both longer and shorter wavelengths than those probed by *Spitzer* in de Wit et al. (2016) will help to better constrain the physical processes shaping HD 80606b atmosphere during its periapse passage. As seen in Figure 9, predicted and observed phase variations for HD 80606b near the periapse of its orbit have a strong dependence on both wavelength and assumptions regarding the chemistry and bulk rotation period of the atmosphere. In particular, observations at wavelengths longward of  $8 \mu\text{m}$  might better constrain the thermal structure of the planet while observations at wavelengths shortward of  $4.5 \mu\text{m}$  might provide more information regarding the formation and evolution of clouds in HD 80606b’s atmosphere near periastron passage.

The *James Webb Space Telescope* (JWST), scheduled for launch in October 2018, will have access to wavelengths longer than what is currently available to *Spitzer* during the warm phase of its mission. Figure 10 shows predicted phase variations using our twice-nominal rotation period model for HD 80606b in four *Spitzer* bandpasses that will be accessible to JWST. We focus here on the twice-nominal rotation period model because it provides the best match to currently available observational data and is in line with the rotation period estimate presented in de Wit et al. (2016). The predicted signal from HD 80606b at  $24 \mu\text{m}$  is a robust 1500 ppm signal with a peak planet/star flux ratio of nearly 2000 ppm. At these long infrared wavelengths, our predicted phase curves do not depend strongly on the assumed cloud species or its average particle size, but with 100 ppm precision a determination of probable cloud species and rotation period of the planet could be made. Similar determinations could be made from  $16 \mu\text{m}$  observations with stronger variations based on composition and average particle size of any clouds present in HD 80606b’s atmosphere. At both  $16$  and  $24 \mu\text{m}$  JWST observations will likely reveal this secondary ‘bump’, thereby more definitively determining the rotation period of HD 80606b, key for understanding tidal dissipation and spin-synchronization for exoplanets.

In the warm phase of its mission, *Spitzer* can provide exceptionally stable long temporal baseline photometry at both  $3.6$  and  $4.5 \mu\text{m}$ . Although  $3.6 \mu\text{m}$  observations of HD 80606b were obtained by *Spitzer*, the systematics present in the data have prevented a full reduction and analysis. Figure 10 shows that the expected signal from HD 80606b at  $3.6 \mu\text{m}$  will be on the order of a few hundred ppm, which is challenging for *Spitzer* but should be achievable with JWST. Both the  $3.6 \mu\text{m}$  and  $5.8 \mu\text{m}$  wavelength spectroscopic regions could provide valuable insights concerning both the composition and average particle size of any clouds present in HD 80606b, although some ambiguity may still

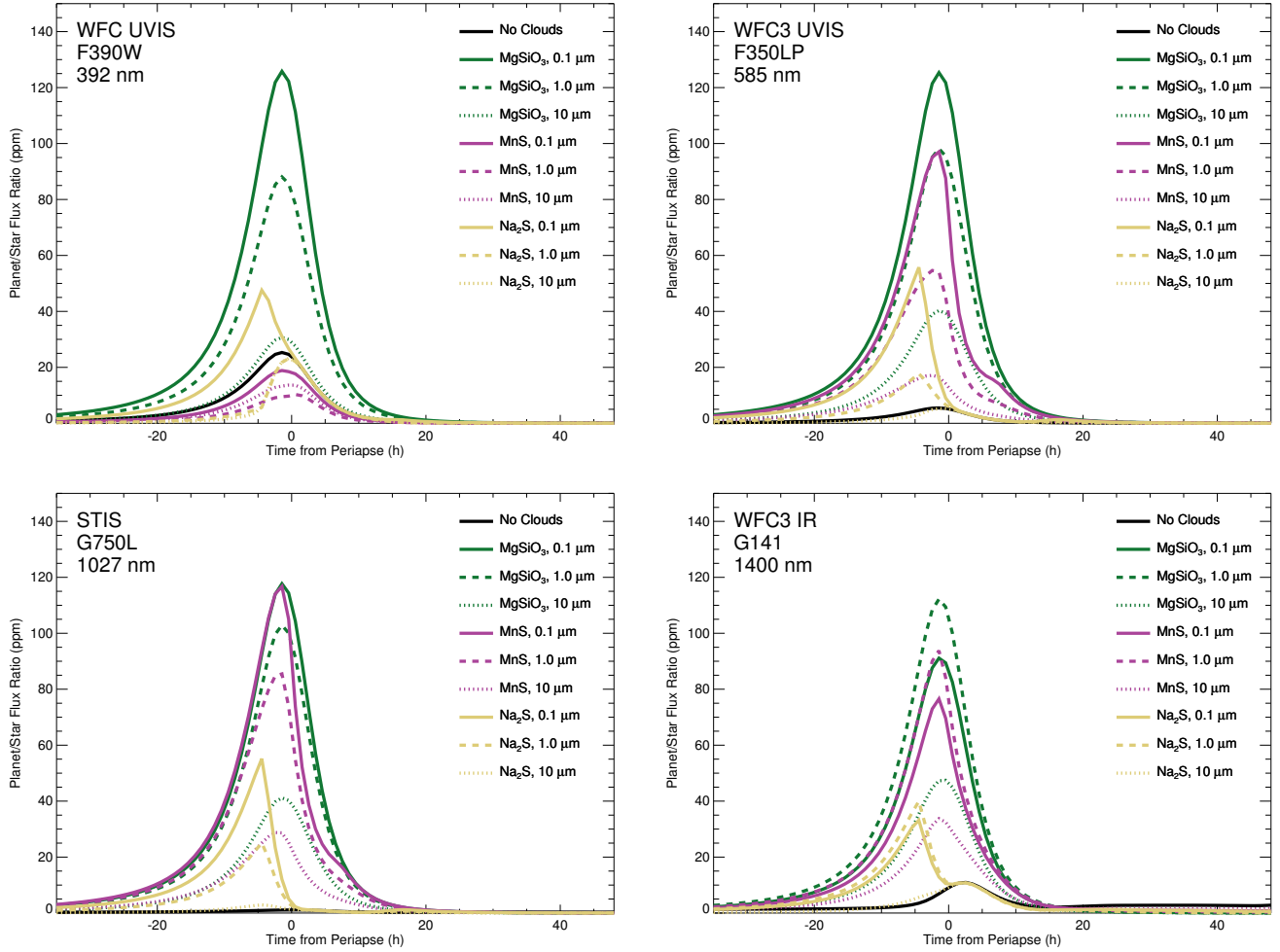


**Figure 11.** Theoretical Planet/Star flux variations for HD 80606b derived from our twice-nominal rotation period model assuming a range of cloud species and particle sizes for a range of potential HST observations. The no cloud (black lines) theoretical phase curves represent contributions due to thermal emission/Rayleigh scattering.

exist. JWST will also provide the potential for spectroscopic exploration of HD 80606b, which could provide further insights into the chemistry, and its relevant timescales, at work in this intriguing atmosphere.

There also exist the potential for observations of HD 80606b near its periapse passage with the *Hubble Space Telescope* (HST). Because HST is in low Earth orbit, it is unable to provide the semi-continuous temporal coverage for phase curve observations that *Spitzer* provides. Despite this fact, a handful of successful exoplanet phase curve studies have been executed with HST (e.g. Stevenson et al. 2014). HST provides for both photometric and spectroscopic observations spanning the far-ultraviolet to the near-infrared. Figure 11 presents a few HST instrument and filter/grism combinations that have the potential to provide high signal-to-noise observations of HD 80606b near secondary eclipse and periastron passage in the optical to near-infrared where scattered light from the planet should dominate the signal. These predictions for HST were derived using our twice-nominal rotation period HD 80606b model for consistency with observations at longer wavelengths, but we see only small variations in our predictions based on assumed rotation period at HST wavelengths.

The signal amplitudes predicted from our models at optical to near-infrared wavelengths are considerably smaller compared with observations at infrared wavelengths (Figure 10), but they have the potential to provide a wealth of critical information concerning the formation and evolution of clouds in HD 80606b’s atmosphere. The cloud-free model predictions presented in Figure 11 have almost vanishingly small amplitudes, but they represent contributions from the planet’s thermal emission (near-infrared) and Rayleigh scattering (blue-visible) at those relevant wavelengths. The presence of clouds would likely dramatically increase the amplitude of any signal from HD 80606b that could be observed with HST.

In the HST bandpasses presented in Figure 11, differences in signals produced by particular cloud species and particle sizes are readily apparent. The amplitude of the predicted HD 80606b phase curve at wavelengths probed by HST depends on a combination of particle size and the particle composition, the case of silicate ( $\text{MgSiO}_3$ ) clouds with a particle size of  $0.1\mu\text{m}$  presenting the most favorable signal at optical to near-infrared wavelengths. The shape of the observed flux variations can give insights into the cloud composition. Clouds that would evaporate during periapse



passage, such as  $\text{Na}_2\text{S}$  clouds, lead to a peculiar triangular-shaped phase curve whereas clouds species that do not evaporate near periapse, such as  $\text{MgSiO}_3$ , have a more symmetrical, bell-shaped phase curve (see also Figure 6). Observations with HST at one or more of the bandpasses presented in Figure 11 of HD 80606b near the periapse of its orbit would provide for the most robust interpretation of cloud properties in its atmosphere.

With a V-band magnitude of 9.0, observations of the HD 80606 system with WFC3-UVIS should yield a 55 ppm precision per 51 sec frame. Therefore, a program targeting HD 80606b's flux modulation around periapse passage at visible wavelengths with HST could allow to disentangle between  $\text{MgSiO}_3/\text{MnS}$  clouds,  $\text{Na}_2\text{S}$  clouds, and a cloud-free atmosphere. It is possible that aerosols not considered in this study (e.g. hazes), would produce a phase curve signature distinct at visible wavelengths. An observation window of 22 hours centered around the periapse passage would yield a sufficient precision on the phase curve shape to constrain the cloud composition. In particular, it should yield a detection of  $1\mu\text{m}$  size  $\text{MgSiO}_3/\text{MnS}$  and  $\text{Na}_2\text{S}$  clouds at the  $\sim 13\sigma$  and  $\sim 7\sigma$  levels, respectively.

## 5. CONCLUSIONS

Our atmospheric models of HD 80606b present a rich area for investigating atmospheric circulation and cloud formation under extreme time-variable forcing conditions. Here we've shown that bulk rotation period assumptions can dramatically alter the atmospheric circulation of a planet like HD 80606b, especially near the periapse of its orbit. We have shown that a number of cloud species could play a significant role in shaping the flux variations of HD 80606b near the periastron of its orbit. In comparing theoretical phase curves for HD 80606b derived from our atmospheric models, we find that our twice-nominal rotation period model with clouds included as an opacity source best match the *Spitzer* observations presented in de Wit et al. (2016).

The de Wit et al. (2016) study used a semi-analytic cloud-free model to constrain the rotation period, radiative timescale, and baseline brightness temperature of HD 80606b from *Spitzer* 4.5 and 8.0  $\mu\text{m}$  observations. de Wit et al. (2016) concluded that the lack of significant flux from the planet outside of the periapse passage region was an indication that HD 80606b's possesses a small internal luminosity. We find that the lack of planetary flux outside of periapse, combined with the timing of the peak planetary flux relative to periapse passage, is more likely an indication of the presence of an optically thick cloud deck composed of material lofted from deep within HD 80606b's atmosphere during periapse passage. This cloud formation and lofting mechanism would work most efficiently in scenarios where HD 80606b has significant internal flux, which provides an important constraint on the tidal and internal evolution of the planet.

In future work, we will include more self-consistent treatment of cloud formation and evolution in our models and an exploration of a larger range of values for the internal temperature and rotation period of HD 80606b. Observations at both shorter and longer wavelengths than those currently available for HD 80606b with JWST and HST would provide more robust constraints on the physical processes at work in HD 80606b's atmosphere. Such atmospheric constraints can then be extended to our global understanding of exoplanet atmospheres and allow us to further refine our models as we begin to explore cooler and smaller worlds beyond our solar system.

NKL thanks H. Wakeford, K. Stevenson, J. Fraine, J. Valenti, S. Hörst, and M. Lewis for their support during the writing of this manuscript. This work was performed in part under contract with the California Institute of Technology (Caltech) funded by NASA through the Sagan Fellowship Program executed by the NASA Exoplanet Science Institute.

## REFERENCES

- Adcroft, A., et al. 2004, *Monthly Weather Review*, 132, 2845  
 Batygin, K., & Stevenson, D. J. 2010, *ApJL*, 714, L238  
 Bodenheimer, P., Lin, D. N. C., & Mardling, R. A. 2001, *ApJ*, 548, 466  
 Cowan, N. B., & Agol, E. 2008, *ApJL*, 678, L129  
 —. 2011, *ApJ*, 726, 82  
 de Wit, J., et al. 2016, *ApJL*, 820, L33  
 Fortney, J. J. 2005, *MNRAS*, 364, 649  
 Fortney, J. J., et al. 2006, *ApJ*, 652, 746  
 —. 2011, *ApJ*, 729, 32  
 —. 2008, *ApJ*, 678, 1419  
 Hut, P. 1981, *A&A*, 99, 126  
 Kataria, T., et al. 2014, *ApJ*, 785, 92  
 —. 2015, *ApJ*, 801, 86  
 —. 2013, *ApJ*, 767, 76  
 —. 2016, *ApJ*, 821, 9  
 Langton, J., & Laughlin, G. 2008, *ApJ*, 674, 1106  
 Laughlin, G., et al. 2009, *Nature*, 457, 562  
 Lewis, N. K., et al. 2014, *ApJ*, 795, 150  
 —. 2010, *ApJ*, 720, 344  
 —. 2013, *ApJ*, 766, 95  
 Marley, M. S., et al. 2013, *Clouds and Hazes in Exoplanet Atmospheres*, ed. S. J. Mackwell, A. A. Simon-Miller, J. W. Harder, & M. A. Bullock, 367–391  
 Marley, M. S., & McKay, C. P. 1999, *Icarus*, 138, 268  
 Morley, C. V., et al. 2012, *ApJ*, 756, 172  
 Moutou, C., et al. 2009, *A&A*, 498, L5  
 Murray, C. D., & Dermott, S. F. 1999, *Solar system dynamics* (Cambridge University Press)  
 Naef, D., et al. 2001, *A&A*, 375, L27  
 Parmentier, V., et al. 2016, *ApJ*, 828, 22  
 Pont, F., et al. 2009, *A&A*, 502, 695  
 Showman, A. P., Cho, J. Y.-K., & Menou, K. 2010, *Atmospheric Circulation of Exoplanets*, ed. Seager, S., 471–516  
 Showman, A. P., et al. 2008, *ApJ*, 682, 559  
 —. 2009, *ApJ*, 699, 564  
 Showman, A. P., & Guillot, T. 2002, *A&A*, 385, 166  
 Showman, A. P., Lewis, N. K., & Fortney, J. J. 2015, *ApJ*, 801, 95  
 Stevenson, K. B., et al. 2014, *Science*, 346, 838  
 Werner, M. W., et al. 2004, *ApJS*, 154, 1  
 Wu, Y., & Murray, N. 2003, *ApJ*, 589, 605